Acta Crystallographica Section B
Structural Science
ISSN 0108-7681

Orientational ordering, tilting and lone-pair activity in the perovskite methylammonium tin bromide, $CH_3NH_3SnBr_3$

Ian Swainson,[a]* Lisheng Chi,[a] Jae-Hyuk Her,[b] Lachlan Cranswick,[a] Peter Stephens,[b] Björn Winkler,[c] Daniel J. Wilson[c] and Victor Milman[d]

[a]Canadian Neutron Beam Centre, National Research Council of Canada, Chalk River, Ontario, Canada K0J 1J0, [b]Department of Physics and Astronomy, State University of New York, Stony Brook, NY 11794-3800, USA, [c]Institut für Geowissenschaften, Fachenheit Mineralogie, Abteilung Kristallographie, Goethe-Universität Frankfurt, Altenhoeferallee 1, D-60438 Frankfurt am Main, Germany, and [d]Accelrys Inc., 334 Science Park, Cambridge CB4 0WN, England

Correspondence e-mail: ian.swainson@nrc.gc.ca

Received 9 December 2009
Accepted 21 April 2010

Synchrotron powder diffraction data from methylammonium tin bromide, $CH_3NH_3SnBr_3$, taken as a function of temperature, reveal the existence of a phase between 230 and 188 K crystallizing in $Pmc2_1$, a = 5.8941 (2), b = 8.3862 (2), c = 8.2406 (2) Å. Strong ferroelectric distortions of the octahedra, associated with stereochemical activity of the Sn $5s^2$ lone pair, are evident. A group analysis and decomposition of the distortion modes of the inorganic framework with respect to the cubic parent is given. The primary order parameters driving this upper transition appear to be an in-phase tilt (rotation) of the octahedra coupled to a ferroelectric mode. The precise nature of the lower-temperature phase remains uncertain, although it appears likely to be triclinic. Density-functional theory calculations on such a triclinic cell suggest that directional bonding of the amine group to the halide cage is coupled to the stereochemical activity of the Sn lone pair *via* the Br atoms, *i.e.* that the bonding from the organic component may have a strong effect on the inorganic sublattice (principally *via* switching the direction of the lone pair with little to no energy cost).

1. Introduction

The term perovskite describes a simple framework structure type with the formula ABX_3, where A is normally a simple cation coordinated by 12 X anions, B a metal coordinated by six X anions, and where the BX_6 octahedra are connected to each other by shared corners to form a three-dimensional framework. The corner-sharing of the octahedra allows for several sets of cooperative rotations, called tilt transitions, leading to a reduction in symmetry from the $Pm\bar{3}m$ aristotype (Glazer, 1972, 1975; Giddy *et al.*, 1993; Hammonds *et al.*, 1998; Howard & Stokes, 1998). Interactions between cation ordering and acoustic modes generate incommensurate phases in many of these compounds (Swainson, 2005).

The first 'hybrid' organic inorganic perovskite appeared 20 years ago (Weber, 1978). These are commonly based on halides of Group 14 elements, Pb, Sn and Ge, occupying the octahedrally coordinated B sites, and organic cations, such as methylammonium (MA), formamidinium (FA) and tetramethylammonium (TMA), which are located in the cages formed by the octahedra. For these perovskites, superlattices may result from an orientational ordering of the organic cations when the ordering is coupled to the orientation and shape of the octahedra.

Going down the periodic table, Group 14 elements have an increasing preference to keep their outer s^2 electron pair as a lone pair, rather than for it to participate in bonding. These lone pairs can become stereochemically active by hybridization (van Aken *et al.*, 2004; Waghmare *et al.*, 2005). The

stereoactivity of the lone pair of the Group 14 elements is often viewed as a class of the Jahn–Teller effect (van Aken *et al.*, 2004; Waghmare *et al.*, 2005; Ra *et al.*, 2003; Seshadri, 2001). However, the origin of the mixed *p* character has been the subject of a debate: does it arise from the mixing of orbitals on the metal atom itself or from mixing with the *p*-orbitals of the anion to which it is octahedrally coordinated? It has been shown that for the chalcogenides of Pb^{2+} (and of the other Group 14 elements), the hybridization is dominated by covalency between *s*-states of the Pb^{2+} atoms with *p* states of the anions (Waghmare *et al.*, 2005; Walsh & Watson, 2005). It remains to be seen whether the same mixing mechanism operates in complex perovksites.

In perovskites the effect of *s*-orbital hybridization of an atom in octahedral coordination is that the atom is driven off-centre, resulting in alternating long and short bonds within the octahedra. As a result, Ge-based analogues exhibit a variety of interesting properties such as ferroelectricity in $CsGeCl_3$ (Christensen & Rasmussen, 1965; Winkler *et al.*, 1988), antiferroelectricity in $TMAGeCl_3$ (Depmeier *et al.*, 1980) and high ionic conductivity in $MAGeCl_3$ (Yamada *et al.*, 1995). In the cubic phases of $MAGeCl_3$ (Yamada *et al.*, 1995), $TMAGeCl_3$ (Yamada *et al.*, 1994) and $TMAGeBr_3$ (Okuda *et al.*, 1996) halide ions are usually modeled occupying the Wyckoff 6*f* site with an occupation factor of 0.50, rather than in the 3*c* site, the typical description of the ideal cubic perovskite. This is due to the presence of dynamical bond switching between Ge—$X\cdots$Ge and Ge$\cdots X$—Ge, *i.e.* the distortion associated with the lone-pair activity is very soft and it is possible that it may be coupled to the dynamic reorientation of the organic cation. Rather than being truly sixfold octahedral, the coordination is often described as pyramidal, $3+3$. ^{35}Cl NQR measurements have shown that the reorientation of the pyramidal $GeCl_3^-$ is the origin of the high ionic conductivity in $MAGeCl_3$ (Yamada *et al.*, 1994, 1995; Okuda *et al.*, 1996; Yamada *et al.*, 2002).

The properties of Sn-based perovskites are expected to be intermediate between those based on Pb and Ge. We have previously examined the local structures of Pb- and Sn-based organic inorganic perovskites using pair-distribution functions derived from synchrotron X-ray scattering. This study shows that the inorganic sublattice of $MASnBr_3$ in the $Pm\overline{3}m$ phase has stronger and more complex local distortions than those of the Pb-based analogues (Worhatch *et al.*, 2007). Long-ranged orientational ordering of the cations in organic inorganic perovskites appears to be inhibited under pressure (Swainson *et al.*, 2007). Generally the lone pair on Pb in octahedral coordination is not strongly stereochemically active, *e.g.* in $MAPbBr_3$ (Swainson *et al.*, 2003). Nevertheless, the off-centring of Pb seen in the octahedra of $MAPbCl_3$ shows that the lone pair can be activated (Worhatch *et al.*, 2007; Swainson *et al.*, 2003; Chi *et al.*, 2005). Di- and trimethylammonium tin bromide have distorted perovskite structures with Sn reported as being $3+3$-coordinated due to lone-pair activity (Thiele & Serr, 1996*a*,*b*). Many Sn-halide perovskites and layer perovskite-like structures have interesting physical properties to which the onset of lone-pair distortions may be coupled; *e.g.* $CsSnBr_3$ is semiconducting at temperatures up to 303 K, above which it shows metal-like behavior (Clark *et al.*, 1981; Narayan & Suryanarayana, 1991).

A calorimetric investigation of $MASnBr_3$ has suggested four possible phase transitions in $MASnBr_3$ at 46, 188.2, 213 and 229.4 K. The 229.4 K transition is also a semiconductor-to-insulator transition (Onoda-Yamamuro *et al.*, 1991), associated with a colour change from red to yellow (Yamada *et al.*, 1988). A differential thermal analysis (DTA) study of the transitions in protonated $MASnBr_3$ (Mori & Saito, 1986) suggested at least two phase transitions on cooling to 160 K.

In this paper we present the results of a diffraction study of $MASnBr_3$ over the temperature range 30–280 K, and a symmetry analysis of the distortion. We also present density-functional theory calculations of the stereochemical activity of the lone pair of Sn^{2+} and its coupling to the directional bonding between the perovskite cage and the MA cation.

2. Experimental

2.1. Sample preparation

$CH_3NH_3SnBr_3$ was synthesized from CH_3NH_3Br and $SnBr_2$, both in anhydrous ethanol solution, as described by Onoda-Yamamuro *et al.* (1991). CH_3NH_3Br (2.0 g) was dissolved in 20 ml of ethanol solution, and then slowly added, drop-by-drop, into 30 ml of a solution of $SnBr_2$, while boiling and stirring. Slow cooling of the solution was accompanied by the precipitation of a deep red solid. All of the operations were carried out in a glove-box filled with He. The solution was then filtered and the precipitate dried for the X-ray experiment. Laboratory X-ray measurements showed that $CH_3NH_3SnBr_3$ is in the $Pm\overline{3}m$ phase at room temperature. The sample was placed in a glass tube, flushed with Ar, and sealed under vacuum for storage and transport to the synchrotron. Before the synchrotron experiment, the powder sample was thoroughly ground by hand to maximize grain sampling by the beam.

2.2. Diffraction data collection

High-resolution X-ray powder diffraction experiments were performed on the X3B1 beamline at the National Synchrotron Light Source, Brookhaven National Laboratory (Balzar *et al.*, 1997). Data were collected at several temperatures in the range 30–280 K, using a closed-cycle helium cryostat. The fine powder sample was mounted on a flat brass plate, 15 mm wide along the incident beam direction, and oscillated by $\pm 2.5^\circ$ about the plate normal during data acquisition. The direct synchrotron beam was monochromated by a Si(111) double-crystal monochromator at a wavelength of $\lambda = 0.700136$ Å. Beyond the sample, the diffracted beam was analyzed by a Ge(111) crystal and detected by a NaI scintillation counter. This configuration gives angular resolution of the order 0.007–0.02° FWHM. λ and $2\theta_0$ were calibrated by measuring a sample of NIST Standard Reference Material 1976 (sintered plate of Al_2O_3).

Table 1
Experimental details for $MASnBr_3$ at 215 K.

Crystal data	
Chemical formula	$CH_3NH_3SnBr_3$
M_r	390.47
Crystal system, space group	$Pmc2_1$
Temperature (K)	215
a, b, c (Å)	5.89406 (17), 8.3862 (2), 8.2406 (2)
V (Å^3)	407.32 (3)
Z	2
Radiation type	Synchrotron, $\lambda = 0.700136$ Å
Specimen shape	Flat plate
Data collection	
Diffractometer	X3B1
Data collection method	Single detector stepwise collection of profile data
Specimen mounting	15 mm wide flat plate
Data collection mode	Reflection
2θ values (°)	$2\theta_{min} = 14.60$, $2\theta_{max} = 41.75$, $2\theta_{step} = 0.004$
Excluded regions	15.7040–16.1200
Refinement	
R factors and goodness of fit	$R_p = 0.093$, $R_{wp} = 0.072$, $R_{exp} = 0.062$, $R_{Bragg} = 0.069$, $\chi^2 = 4.044$
No. of data points	6683
No. of parameters	33
No. of restraints	1
H-atom treatment	H-atom parameters not defined

2.3. Indexing, model generation and refinement methods of diffraction data

Indexing of the low-temperature phases was performed using the *Crysfire* suite of indexing programs (Shirley, 1999). The direct-methods package *EXPO* (Altomare *et al.*, 1993) was used for structure solution from powder diffraction data. Group relationships of the unit cells to tilt structures were examined using the ISOTROPY and ISODISPLACE codes (Stokes & Hatch, 2000; Campbell *et al.*, 2006, 2007). The refinements were performed using *GSAS* (Larson & Von Dreele, 1986). In order to reduce the effect of spill over of the beam from the flat-plate sample at low angles, the data were truncated below 14.5° 2θ during refinement.

2.4. Density-functional theory calculations

DFT calculations were performed using the CASTEP code (Segall *et al.*, 2002). The generalized gradient approximation was employed. The calculations employ a plane-wave basis set in conjunction with ultrasoft pseudopotentials, which were taken from the CASTEP database. For Sn, the 4*d* electrons were included in the frozen core, leaving the $5s^2$ and $5p^2$ electrons as valence electrons. A plane-wave basis set cutoff of 310 eV was chosen. The Pulay stress correction was evaluated numerically by performing total energy calculations at three different values of the kinetic energy cutoff. Calculations were performed using eight **k** points in the reduced wedge of the Brillouin zone. Calculations were considered converged when the following four conditions were met: the change in energy/atom < 5 meV residual, the forces on the atoms < 0.01 eV Å^{-1}, the displacements of atoms during the geometry optimization steps < 0.0005 Å, and the residual bulk stress < 0.02 GPa.

3. Results and discussion

3.1. Diffraction

The synchrotron diffraction pattern of $MASnBr_3$ contained several weak impurity peaks. These impurity lines were determined at the beginning of the experiment in the cubic phase, where peak density from the sample was sparse, and were excluded in indexing attempts in the lower temperature phases. Indexing of the pattern taken at 215 K yielded an orthorhombic cell of approximately 5.891, 8.386, 8.241 Å, whose cell sides are related to a_P, the cubic cell, by (a_P, $(2)^{1/2}a_P$, $(2)^{1/2}a_P$). The systematic absence conditions suggested that the most likely space group was $Pmc2_1$. The octahedron was located within the unit cell by the direct methods program *EXPO* (Altomare *et al.*, 1993). The MA ion was represented as a rigid C—N rod of 1.48 Å, and the H atoms ignored during refinement. The cell parameters and agreement factors for this phase are listed in Table 1. $\delta(r)$, the displacement of the Sn from the centroid, and V_0, the volume of the tin bromide octahedron, were calculated as 0.12 Å and 35.290 Å^3, using *IVTON* (Balic Žunić & Vicković, 1996). It is not possible to apply the current bond-valence calculations fully to this structure, as we have not established the H positions, nor are there established parameters for such interactions as H···Br, if we had. However, such calculations were performed on the inorganic sublattice, with R_0 and b, cutoff and softness difference of 2.37369, 0.501, 6.0 and 0.11066, respectively, using the software *softBV* (Orlov & Popov, 2004). With Sn—Br bond lengths between 2.676 and 3.306 Å, the valence sum to Sn is 1.9972 v.u. (valence units), in good agreement with its nominal divalence. The three Br atoms have valence sums of

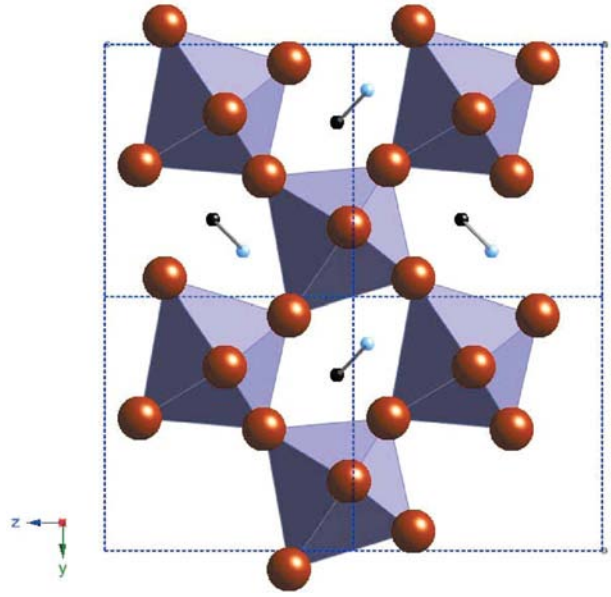

Figure 1
View of the $Pmc2_1$ phase at $T = 215$ K down the *a* axis, which is related to the unique tilt axis of the $P4/mbm\ a^0a^0c^+$ tilt system. The tilts of the octahedra are in phase down this axis. The large brown spheres are Br atoms, the small black and cyan atoms are C and N, respectively. Sn is not shown and lies near the centroid of the octahedron (shaded purple). This figure is in colour in the electronic version of this paper.

Table 2
Internal mode decomposition of the inorganic framework of the $Pmc2_1$ structure with respect to an ideal $Pm\bar{3}m$ parent, in which Sn sits on the Wyckoff *a* sites at (0, 0, 0) and Br on the *d* sites at ($\frac{1}{2}$, 0, 0).

Subgroup: $Pmc2_1$, basis = {(0, 0, 1), (1, −1, 0), (1, 1, 0)}, origin = ($\frac{1}{2}$, 0, 0), $s = 2$, $i = 24$.

k-point	IR†	Direction	Space group	Size‡	Index§	Site: Wyckoff	Mulliken¶ (branch)	Amplitude (Å)
[0, 0, 0]	Γ_4^-	(*a*, *a*, 0)	*Amm*2	$s = 1$	$i = 12$	[Sn: *a*]	$T_{1u}(a)$	0.20260
						[Br: *d*]	$A_{2u}(a)$	0.44805
						[Br: *d*]	$E_u(a)$	0.13883
[0, 0, 0]	Γ_5^-	(0, *a*, −*a*)	*Amm*2	$s = 1$	$i = 12$	[Br: *d*]	$E_u(a)$	−0.06336
[$\frac{1}{2}$, $\frac{1}{2}$, 0]	M_2^+	(*a*, 0, 0)	*P*4/*mbm*	$s = 2$	$i = 6$	[Br: *d*]	$A_{2u}(a)$	−0.02117
[$\frac{1}{2}$, $\frac{1}{2}$, 0]	M_3^+	(*a*, 0, 0)	*P*4/*mbm*	$s = 2$	$i = 6$	[Br: *d*]	$E_u(a)$	−0.57797
[$\frac{1}{2}$, $\frac{1}{2}$, 0]	M_5^-	(0, 0, 0, *a*, 0, 0)	*Pmma*	$s = 2$	$i = 12$	[Sn: *a*]	$T_{1u}(a)$	0.00984
						[Br: *d*]	$E_u(a)$	−0.20670

† Irreducible representation, using the labelling of Miller & Love (1967). ‡ Size of the primitive unit cell with respect to the parent $Pm\bar{3}m$ cubic cell. § Index of the subgroup with respect to the parent: the ratio of the number of symmetry elements. ¶ The Mulliken label for the site symmetry of the distortion. The (*a*) refers to the *a* contained in the order parameter direction: all are one-dimensional order parameters.

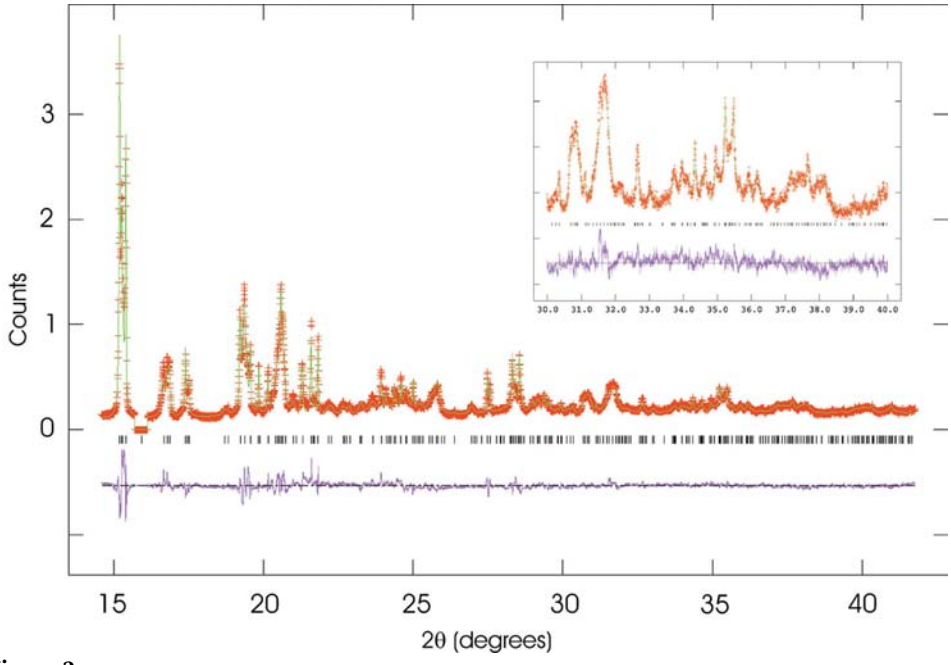

Figure 2
Rietveld analysis results for the $Pmc2_1$ intermediate phase. The crosses represent observed data, the solid line the calculated pattern, the bottom line the difference, while vertical marks indicate Bragg peaks. The vertical axis is in units of thousands of counts. Inset: an expanded view of the fit at high 2θ over the range 30–40° 2θ.

0.7041, 0.6683 and 0.6247. This gives some idea of the required valence strength from the methylammonium group.

The structure viewed down [100] is shown in Fig. 1, and the fit to the data in Fig. 2. The MA ion is ordered in the $Pmc2_1$ phase and the lone pair is stereochemically active. Both $SnBr_6$ octahedra and MA molecules reside on mirror planes.

3.2. Mode decomposition and group analysis

Far more information than the geometric description of the distortion of an octahedron can be gained by examining both the internal distortions of the octahedron and the whole body rotations and translations of the inorganic component of the structure in terms of group theory. A post-refinement mode decomposition of the $Pmc2_1$ structure with respect to the parent was performed on the inorganic framework component of the perovskite, with the ISODISPLACE code (Campbell *et al.*, 2006, 2007). The irreducible representations involved in the change of symmetry from $Pm\bar{3}m$ to $Pmc2_1$ are calculated together with their basis functions. The amplitudes, defined with respect to the parent structure, of these potential basis vectors, which are by definition orthogonal functions, are then fitted against the observed structure. Ignoring the strains, the results for the internal distortions of the cells are given in Table 2. The notation for output consists of: the parent space group; the **k** point in the Brillouin zone; the label of the irreducible representation (in the system of Miller & Love, 1967); the order parameter direction (in essence, a measure of the proportion of the possible symmetry that may be broken by the representation which is actually broken); the subgroup that would be induced if that representation acted alone; *s*, the size of the primitive unit cell compared with that of the parent; *i*, the ratio of symmetry elements of the parent to the subgroup, followed by the atoms that are involved and the Wyckoff sites on which these atoms sit in the parent cell; the point group label for the distortion; the branch of the order parameter involved (there is only one branch, *a*, for each of these modes in this case); and an amplitude of the distortion in Å. The notation is fully discussed by Campbell *et al.* (2006, 2007).

No single irreducible representation can trigger this phase transition. The order parameter with the largest amplitude transforms as $M_3^+(a, 0, 0)$, which if acting in isolation would trigger the pure tilt transition to *P*4/*mbm* (Table 2; Howard & Stokes, 1998). Its presence in the decomposition is not surprising as *P*4/*mbm* is the first non-cubic phase encountered on cooling the alkali analog $CsSnBr_3$ (Mori & Saito, 1986). There are eight possible combinations of two primary order parameters that could produce this $Pmc2_1$ structure, of which the likeliest combination involves the tilt instability

Table 3
Comparison of cell volumes and energies from CASTEP and distortions of octahedra.

δ_r gives the distance of the Sn atom from the geometric centre of the octahedron. V_o is the volume of the octahedron, V the volume of the unit cell, and E, the total energy.

	Model 1	Model 2	Model 3	Model 4
Sn1—Br1 (Å)	3.3708	3.2374	3.2652	3.09646
Sn1—Br2 (Å)	2.8315	3.0006	2.8853	3.05119
Sn1—Br3 (Å)	2.9350	2.8338	2.8326	2.80421
Sn1—Br3 (Å)	2.9995	3.1361	3.1629	3.25912
Sn1—Br5 (Å)	2.7961	2.8348	2.8250	2.93797
Sn1—Br6 (Å)	3.2224	2.9992	3.1603	2.94138
V_o (Å)	36.281	35.845	36.653	36.166
δ_r (Å)	0.250	0.197	0.135	0.144
Sn2—Br1 (Å)	2.8259	2.8888	2.8286	2.89487
Sn2—Br2 (Å)	3.1487	2.8850	3.3763	3.06072
Sn2—Br4 (Å)	2.8260	2.8644	2.7861	2.77225
Sn2—Br4 (Å)	3.1225	3.1260	3.2319	3.30050
Sn2—Br5 (Å)	3.3129	3.2020	3.3069	3.18070
Sn2—Br6 (Å)	2.9139	3.1216	2.8143	2.94905
V_o (Å^3)	36.351	36.191	37.815	36.534
δ_r (Å)	0.250	0.126	0.177	0.210
a (Å)	8.7583	8.6165	8.7166	8.6050
b (Å)	8.3749	8.3871	8.4465	8.3672
c (Å)	5.9305	5.9502	5.9926	6.0330
α (°)	85.755	91.453	88.563	91.117
β (°)	91.509	90.420	91.286	92.741
γ (°)	90.914	90.892	90.082	90.448
V (Å^3)	433.62	429.80	440.95	433.78
E (eV)	−3438.359	−3438.342	−3438.341	−3438.335

$M_3^+(a,0,0)$ coupled with the ferroelectric mode $\Gamma_4^-(a,a,0)$, which are also the two modes with the largest amplitudes (this ignores the order–disorder phenomenon associated with the MA cation). In this scenario, the other distortion modes in Table 2 are secondary order parameters in that they do not break any additional symmetry. The largest amplitude distortion modes are shown schematically in Fig. 3. There are more distortion modes affecting displacements of Br than of Sn, and the displacements of Br also have the largest amplitudes.

The Sn—Br bond distances in the $Pmc2_1$ cell are alternately long and short along [011] and $[0\bar{1}1]$, primarily owing to the large amplitude of the $\Gamma_4^-(a,a,0)[\mathrm{Br}:d]A_{2u}(a)$ mode (Table 2); the third pair of Sn—Br bonds along the a axis remain equivalent by symmetry.

3.3. Diffraction at lower temperatures

A rhombohedral cell has been deduced from the neutron difffraction data of $CD_3ND_3SnBr_3$ taken at 195 K (Onoda-Yamamuro *et al.*, 1995). We carefully monitored 100, 110 and 111 peaks between 188 and 230 K on cooling and heating for several cycles in our protonated sample: we only found the orthorhombic cell. It is possible that a strong isotope effect exists in $MASnBr_3$, since this is the only difference between the two samples in the two experiments, and strong isotope effects on phase boundaries are known in $MAGeCl_3$ (Yamada *et al.*, 2002): *e.g.* by 475 K (a few degrees below its melting point) only 7% of $CD_3ND_3GeCl_3$ transforms to the cubic phase, while the rest of the sample remains rhombohedral, whereas $CH_3NH_3GeCl_3$ transforms entirely to the cubic phase by 349 K (Yamada *et al.*, 2002). This shows that the inorganic component of the structure of these compounds is highly sensitive to subtle changes in the strength of interactions with the MA cation – a point we shall examine further.

Of the many cells we examined for the 30 K data, the best candidate was a triclinic cell, $a = 8.345$, $b = 8.135$, $c = 5.899$ Å, $\alpha = 92.14$, $\beta = 89.95$, $\gamma = 91.42°$ and $V = 400.06$ Å^3, with the same basis as the orthorhombic cell. We assumed a lack of inversion centre, as the orthorhombic supercell lacks one: with the space group $P1$ there are two independent $SnBr_6$ octahedra, and two MA cations in this candidate cell.

4. DFT calculations of the candidate triclinic phase

Many detailed studies on the chalcogenides of Group 14 elements have demonstrated conclusively that overlapping orbitals from the anions are responsible for the ultimate mixing of p-characteristics with the ns^2 orbitals. Our intention here was not to look at specific orbital overlap in the inorganic framework, but to look at the qualitative effect of the organic component on the inorganic framework itself.

The refinement using the low-temperature X-ray data was far less satisfactory than that of the orthorhombic phase; the

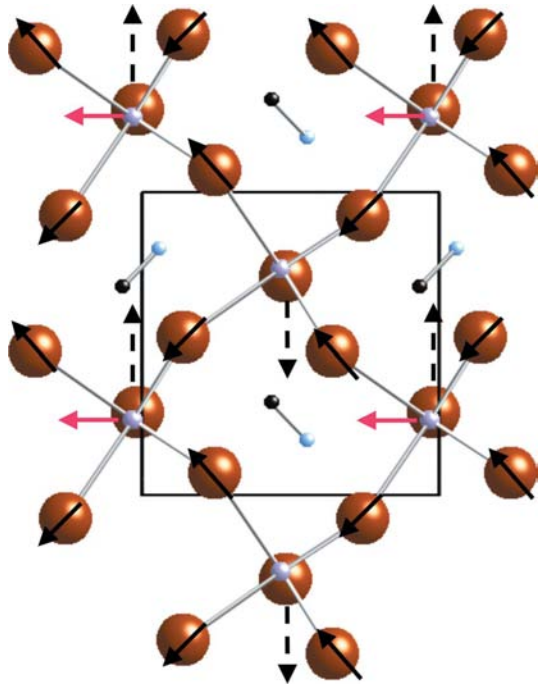

Figure 3
View of the $Pmc2_1$ phase at $T = 215$ K down the a axis, with the top Br of the octahedron omitted. The principal distortion modes from the mode decomposition (Table 2) larger than a magnitude of 0.15 are shown with $\Gamma_4^-[\mathrm{Br}:d]A_{2u}$ (solid black arrow), affecting the equatorial bromines lying near the 100 plane, $M_5^-[\mathrm{Br}:d]E_u$ (dashed black arrow) displacing the axial bromines running along the a axis, and $\Gamma_4^-[\mathrm{Sn}:a]T_{1u}$ (pink arrow) showing the displacement of the Sn atom itself. The $M_3^+[\mathrm{Br}:d]E_u$ mode (no arrows) governs rigid rotation of the octahedra. This figure is in colour in the electronic version of this paper.

best fit that we achieved was $R_p = 0.12$ and $R_{wp} = 0.15$. From this refinement it would be difficult to claim that we have definitively solved the structure of the low-temperature phase. Nevertheless, this cell, with its absence of symmetry constraints is a very flexible medium in which to examine the strength and nature of the interactions between the organic and inorganic sublattices. The starting parameters for the DFT trials were taken from the synchrotron diffraction data: the cell was that indexed to the 30 K diffraction data, and the contents were projected into it from the 215 K refinement. In total four trials were performed in which all four combinations of flipping the two MA ions head-to-tail in the same starting *P*1 cell were tested, and the energy of the cell minimized by a full geometry optimization (Table 3). The total energies of the relaxed structures agree within 0.023 eV and are hence equal within the numerical uncertainty of the calculations. Surprisingly however, differences in the unit-cell volume are up to 2.5%.

Comparison of the four minimized states shows several interesting trends. During the lattice relaxation, one response to the head-to-tail flipping of the MA ions was that they drifted through the *A*-site cavity, due to the attraction between Br and the amine group. One can use the DFT analysis to visualize interactions between atoms; the difference electron density function (representing the difference between the self-consistent charge density and the electron distribution obtained by a superposition of non-interacting atoms located at the same positions as in the geometry-optimized structure) shows the expected polarization of both the electrons towards N in the C—N bond of MA and of the electrons from Br towards H atoms on the amine end of the MA cation (Fig. 4).

^{119}Sn Mössbauer spectroscopy suggests that the smaller isomer shifts at 93 K compared with those at 293 K, and the observation of quadrupolar splitting, arise from the decrease in pure *s*-electron density due to hybridization with *p*-orbitals (Yamada *et al.*, 1988). The effect of this non-spherical lone pair can be seen indirectly by its effect on the bond lengths, and directly by calculating the electron density distribution within DFT-relaxed lattices. The hybridized lone pair can be seen localized preferentially opposite the short tin bonds (Fig. 5).

Table 3 shows that while some interatomic distances (such as Sn1Br1) are consistently long in all models, and other sets are consistently short (such as Sn1Br3) others show a high degree of variation, the extreme case being Sn2Br2. In all cases there were two distinct tin environments with charges of 0.68 (1) on Sn1 and 0.72 (1) on Sn2. There is strong coupling between the orientation of the MA cation and the lone pair on Sn^{2+}, which appears to be mediated by Br, to which Sn is bonded in the octahedron and to which the MA cation is hydrogen bonded. There are significant differences between models in the distortions of the $SnBr_6$ octahedra and in unit-cell volumes. However, the charges on the Sn atoms and the

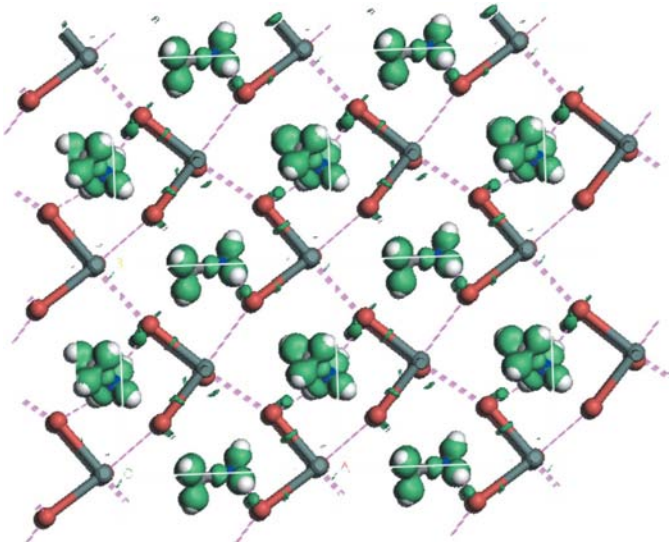

Figure 4
Electron difference-density distribution with contour values of 0.045 e Å^{-3} overlain on a ball and stick plot of the unit cell of a DFT-relaxed *P*1 structure. Bromines are in red and the MA molecular cation lies in the cavity. Polarization of the electrons along the C—N bond within the MA ion towards the N atom (blue) can be seen, and electrons are drawn from the Br atom towards the partly unshielded H on the amine, seen as a lobe of electron density protruding off Br. Only the shorter Sn—Br bonds are drawn with sticks; the other Sn—Br bonds, drawn without sticks, are elongated, due to repulsion from the lone pair on Sn.

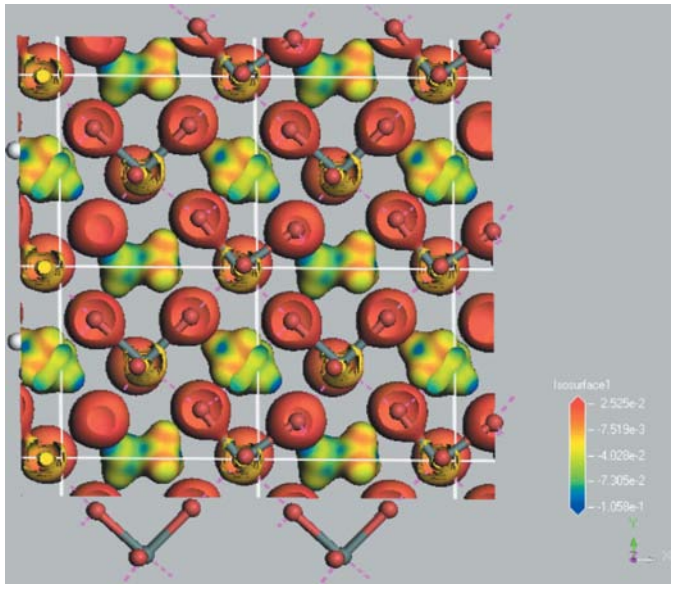

Figure 5
Electron-density difference distribution with contour values of 0.227 e Å^{-3}. This is overlain on a 2 × 2 ball-and-stick plot of the unit cell of a DFT-relaxed *P*1 structure of $MASnBr_3$ (Model 2 of Table 3). The bromine atoms are in red (coinciding with the colour of their surrounding electron difference density), MA is in the cavity (in which the internal polarization can be seen as mottled colors) and tin (atom color gray) sits near the corners and the centres of the unit cell. Around the Sn atom, the anisotropic distribution of hybridized *s*-electron density can be seen (broken yellow distribution). Two short Sn—Br distances (represented with sticks) are on the opposite side of the Sn atom from the maxmium of the electron density of the $5s^2$ lone pair. Due to repulsion, the Sn—Br bonds situated nearer the maximum of the lone-pair distribution are longer: no sticks are drawn to represent these bonds.

Table 4
Average geometry of methylammonium geometry in the four DFT models.

Δ *trans* gives the r.m.s. distortion (in °) from the methyl group being in a *trans* configuration with the amine.

C—H (Å)	1.0948 (5)	N—H	1.046 (6)
H—C—H	110.2 (2)	H—N—H	107.3 (9)
Δ *trans*	1.8	C—N	1.4917 (9)

enthalpies (Table 3) are not significantly different between models.

While it is quite likely that none of these cells represent the true ground state, these results suggest that static disorder of different distortional variants is quite possible. This may also be a reason for the poorer fit to the 30 K diffraction data, as only one long-range model was assumed in the Rietveld refinement, and multiphase refinements of near-identical triclinic phases are not stable. Even in the $Pm\bar{3}m$ phase, the local structure of the inorganic sublattice of $MASnBr_3$ is far more complex than those observed for the Pb-based analogs (Worhatch *et al.*, 2007). Some of this short-range structure may well be due to dynamic interactions between organic and inorganic components. Apart from evidence in $MASnBr_3$ itself, there are other reasons to think that there may be several coexisting variants by analogy to methylammonium germanium chloride, where extremely subtle differences in interactions from the MA cation with the inorganic sublattice are responsible for the strong isotope effect between $CD_3ND_3GeCl_3$ and $CH_3NH_3GeCl_3$ (Yamada *et al.*, 2002); two phases of different symmetries coexist over a broad temperature range in $CD_3ND_3GeCl_3$, an effect which does not occur in $CH_3NH_3GeCl_3$.

Rigid-body constraints have been used to describe the MA cation to both solve and refine crystal structures from neutron powder data where the resolution required constraints for the complexity of the problem (Swainson *et al.*, 2003; Chi *et al.*, 2005). The DFT-relaxed lattices were used to examine the variability of the geometry of the MA cation, and C—H bond lengths of 1.0948 (5) Å and N—H bond lengths of 1.046 (6) Å are observed (Table 4). The greater variability of the N—H lengths reflects variability of the interactions between the amine and Br atoms. The average deviation from a *trans* conformation is less than 2°. Therefore, rigid-body constraints are reasonable for refinements of orientationally ordered phases and if only partial relaxation of this constraint is required, it would be best to relax the amine group. The geometry of the MA ion (Table 4) is far more consistent than that of the inorganic component of the structure (Table 3).

5. Conclusions

A synchtrotron diffraction study was undertaken on methylammonium tin bromide, an organic inorganic system in which the inorganic sublattice exhibits tilting of the octahedra and lone-pair distortions on the Sn atom, coupled to orientational ordering of the amine cation in the distorted cage. We found three phases of $MASnBr_3$ from room temperature to 30 K. The structure at room temperature is that of the untilted $Pm\bar{3}m$ perovskite, in which the amine must be disordered, owing to the high site symmetry. The structure of the intermediate phase of $MASnBr_3$ was solved and refined and is orthorhombic, $Pmc2_1$, with strong distortions of the octahedra. This is associated with a lone-pair distortion of the electron distribution on the Sn atom. The lowest temperature phase remains uncertain, although the likeliest candidate cell is triclinic. We saw no perceptible structural changes at 46 K or 213 K, which had been reported as potential transition temperatures from calorimetry studies.

The DFT calculations demonstrate that quite distinct and strong distortions of the inorganic framework have nearly identical energies. In $MASnBr_3$ the directional hydrogen bonding between the amine and the Br atoms appears to couple to both the tilts of the octahedra as well as the stereoactive lone pair of the Sn^{2+} cation; the factor correlating these may be Br, which is affected by the hydrogen bonding and the hybridization of the Sn *s* orbitals. While in all cases the organic cation remains nearly ideal in geometry, the inorganic framework is clearly very soft. These calculations demonstrate the plausibility of switching the orientation of the lone pair on Sn^{2+} in response to reorientation of the nearly rigid organic cations. The results of these static lattice relaxations parallel the still stronger, and dynamic, switching of the orientation of the lone pair on Ge^{2+} observed in cubic $MAGeCl_3$ (Yamada *et al.*, 1994, 1995, 2002; Okuda *et al.*, 1996).

L. Chi thanks the National Science and Engineering Research Council (NSERC) of Canada for a Visiting Fellowship in Canadian Government Laboratories. IPS gratefully acknowledges the NSLS and JW Goethe-Universität Frankfurt for their hospitality and assistance.

References

Aken, B. B. van, Palstra, T. T. M., Filippetti, A. & Spaldin, N. A. (2004). *Nature Mater.* **3**, 164–170.
Altomare, A., Cascarano, G., Giacovazzo, C. & Guagliardi, A. (1993). *J. Appl. Cryst.* **26**, 343–350.
Balić Žunić, T. & Vicković, I. (1996). *J. Appl. Cryst.* **29**, 305–306.
Balzar, D., Stephens, P. W. & Ledbetter, H. (1997). *Fizika A*, **6**, 41–50.
Campbell, B. J., Evans, J. S. O., Perselli, F. & Stokes, H. T. (2007). *IUCr CompComm. Newsl.* **8**, 81–95.
Campbell, B. J., Stokes, H. T., Tanner, D. E. & Hatch, D. M. (2006). *J. Appl. Cryst.* **39**, 607–614.
Chi, L., Swainson, I. P., Cranswick, L. M. D., Her, J.-H., Stephens, P. W. & Knop, O. (2005). *J. Solid State Chem.* **178**, 1376–1385.
Christensen, A. N. & Rasmussen, S. E. (1965). *Acta Chem. Scand.* **19**, 421–428.
Clark, S. J., Flint, C. D. & Donaldson, J. D. (1981). *J. Phys. Chem. Solids*, **42**, 133–135.
Depmeier, W., Möller, A. & Klaska, K.-H. (1980). *Acta Cryst.* B**36**, 803–807.
Giddy, A. P., Dove, M. T., Pawley, G. S. & Heine, V. (1993). *Acta Cryst.* A**49**, 697–703.
Glazer, A. M. (1972). *Acta Cryst.* B**28**, 3384–3392.
Glazer, A. M. (1975). *Acta Cryst.* A**31**, 756–762.
Hammonds, K. D., Bosenick, A., Dove, M. T. & Heine, V. (1998). *Am. Mineral.* **83**, 476–479.
Howard, C. J. & Stokes, H. T. (1998). *Acta Cryst.* B**54**, 782–789.

Larson, A. C. & Von Dreele, R. B. (1986). *GSAS.* Technical Report LAUR 86–748. Los Alamos National Laboratory, New Mexico, USA.
Miller, S. C. & Love, W. F. (1967). *Tables of Irreducible Representations of Space Groups and Co-Representations of Magnetic Space Groups.* Boulder: Pruett Press.
Mori, M. & Saito, H. (1986). *J. Phys. Solid State Phys.* **19**, 2391–2401.
Narayan, R. L. & Suryanarayana, S. V. (1991). *Mater. Lett.* **11**, 305–308.
Okuda, T., Gotou, S., Takahashi, T., Terao, H. & Yamada, K. (1996). *Z. Naturforsch.* **51**, 686–692.
Onoda-Yamamuro, N., Matsuo, T. & Suga, H. (1991). *J. Chem. Thermodyn.* **23**, 987–989.
Onoda-Yamamuro, N., Yamamuro, O., Matsuo, T., Suga, H., Oikawa, K., Tsuchiya, N., Kamiyama, T. & Asano, H. (1995). *Physica B*, **213–214**, 411–413.
Orlov, I. P. & Popov, K. (2004). *softBV*, Version 0.96, http://kristall.uni-mki.gwdg.de/softbv/index.html.
Ra, H.-S., Ok, K. M. & Halasyamani, P. S. (2003). *J. Am. Chem. Soc.* **125**, 7764–7765.
Segall, M. D., Lindan, P. J. D., Probert, M. J., Pickard, C. J., Hasnip, P. J., Clark, S. J. & Payne, M. C. (2002). *J. Phys. Condens. Matter*, **14**, 2717–2744.
Seshadri, R. (2001). *Proc. Indian Acad. Sci. Chem. Sci.* **113**, 487–496.
Shirley, R. (1999). *CRYSFIRE Suite.* Surrey, England: The Lattice Press.
Stokes, H. T. & Hatch, D. M. (2000). *ISOTROPY*, 6th ed. Brigham Young University, UT, USA.
Swainson, I. P. (2005). *Acta Cryst.* B**61**, 616–626.
Swainson, I. P., Hammond, R. P., Soulliere, C., Knop, O. & Massa, W. (2003). *J. Solid State Chem.* **176**, 97–104.
Swainson, I. P., Tucker, M. G., Wilson, D. J., Winkler, B. & Milman, V. (2007). *Chem. Mater.* **19**, 2401–2405.
Thiele, G. & Serr, B. R. (1996*a*). *Z. Kristallogr.* **211**, 47.
Thiele, G. & Serr, B. R. (1996*b*). *Z. Kristallogr.* **211**, 46.
Waghmare, U. V., Spaldin, N. A., Kandpal, H. C. & Seshadri, R. (2005). *Phys. Rev. B*, **67**, 125111.
Walsh, A. & Watson, G. W. (2005). *J. Phys. Chem. B*, **109**, 18868–18875.
Weber, D. (1978). *Z. Naturforsch. B*, **33**, 862.
Winkler, B., Milman, V. & Lee, M.-H. (1988). *J. Chem. Phys.* **108**, 5506–5509.
Worhatch, R. J., Kim, H.-J., Swainson, I., Yonkeu, A. & Billinge, S. (2007). *Chem. Mater.* **20**, 1272–1277.
Yamada, K., Isobe, K., Okuda, T. & Furukawa, Y. (1994). *Z. Naturforsch. A*, **49**, 258–266.
Yamada, K., Isobe, K., Tsuyama, E., Okuda, T. & Furukawa, Y. (1995). *Solid State Ionics*, **79**, 152–157.
Yamada, K., Mikawa, K., Okuda, T. & Knight, K. S. (2002). *J. Chem. Soc. Dalton Trans.* pp. 2112–2118.
Yamada, K., Nose, S., Umehara, T., Okuda, T. & Ichiba, S. (1988). *Bull. Chem. Soc. Jpn*, **61**, 4265–4268.